We are IntechOpen,
the world's leading publisher of
Open Access books
Built by scientists, for scientists

6,900
Open access books available

186,000
International authors and editors

200M
Downloads

Our authors are among the

154
Countries delivered to

TOP 1%
most cited scientists

12.2%
Contributors from top 500 universities

CLARIVATE ANALYTICS
BOOK CITATION INDEX
INDEXED

WEB OF SCIENCE™

Selection of our books indexed in the Book Citation Index
in Web of Science™ Core Collection (BKCI)

Interested in publishing with us?
Contact book.department@intechopen.com

Numbers displayed above are based on latest data collected.
For more information visit www.intechopen.com

Superconductivity and Electron-Phonon Coupling in Graphite Intercalation Compunds

Tonica Valla and Zhihui Pan
Condensed Matter Physics and Materials Science Department, Brookhaven National
Laboratory
USA

1. Introduction

In graphite intercalation compounds (GIC), the intercalation of various atomic or molecular species in between graphene layers in graphite leads to novel properties and a very rich physics, including superconductivity (Dresselhaus & Dresselhaus, 2002). In graphite intercalated with alkaline metals, superconductivity has been known for decades (Hannay et al., 1965), but after recent discovery of relatively high T_c superconductivity in CaC_6 ($T_c = 11.5$ K)(Emery et al., 2005; Weller et al., 2005) research in this field has been intensified. In conventional metals, the electron-phonon coupling has long been known to be the pairing interaction responsible for the superconductivity. The strength of this interaction essentially determines the superconducting transition temperature T_c. Even though the electron-phonon coupling is most likely responsible for pairing in GICs (Hinks et al., 2007; Kim et al., 2006; Lamura et al., 2006), it is still not clear what electronic states, intercalant- or graphene- derived ones, and what phonons are responsible for pairing (Boeri et al., 2007; Calandra & Mauri, 2005; Mazin et al., 2007; Mazin, 2005). Due to differences in structure and composition, no clear trends have been identified that could unambiguously resolve these issues. For example, KC_8 is a superconductor and LiC_6 is not. Further, in GICs intercalated with alkaline earths, T_c ranges from zero to 11.5K, even though they share the same chemical formula MC_6, where M is an alkaline earth atom. This obviously represents a serious problem to the proposal that superconductivity originates from graphene sheets and that the only role of intercalants is to provide the charge to the graphene bands. Further, band structure calculations show that in graphite and GICs, an interlayer state exists above π^* band (Holzwarth et al., 1984; Posternak et al., 1983), prompting some researchers to propose that its partial filling and coupling to soft intercalant phonons induces superconductivity in GICs (Csányi et al., 2005; Mazin, 2005). The experimental situation is still inconclusive, with strong advocates for intercalant (Hinks et al., 2007) and graphene dominated superconductivity (Dean et al., 2010; Grüneis et al., 2009; Kim et al., 2006; Pan et al., 2010; Valla et al., 2009). Recent angle resolved photoemission spectroscopy study on CaC_6 (Valla et al., 2009) reported that the electron-phonon coupling on graphene-derived Fermi surface to graphene phonons is strong enough to explain a T_c in the range of tens of Kelvin, indicating that graphene sheets provide crucial ingredients for superconductivity in GICs. However, to test this idea, it would be important to extend similar studies to GICs with different T_c.

One manifestation of electron-phonon coupling is a renormalization of the electronic dispersion or a "kink" at the energy scale associated with the phonons. This renormalization

is directly observable in a photoemission experiment, making photoemission spectroscopy an ideal probe of electron-phonon coupling. In this chapter, we present the angle resolved photoemission studies of the electronic structure and the electron-phonon coupling in the non-superconducting LiC_6 and in superconducting KC_8 ($T_c = 0.39$ K) and compare these materials with several other GICs. We find that the electron-phonon coupling on the graphene derived π^* states to the graphene derived phonons increases with the filling of π^* states in a sequence from LiC_6 to KC_8 to CaC_6, following the same trend as T_c. The positive correlation between these quantities implies that superconductivity originates in graphene sheets while the main role of intercalants is to provide the charge for filling of the graphene π^* states.

2. Photoemission and interactions

In photoelectron spectroscopy, a photon of known energy, $h\nu$, is absorbed and the outgoing electron's kinetic energy $E_K = h\nu - \phi - \varepsilon_k$ and angle are measured. These properties determine the binding energy ε_k and parallel momentum $k_\parallel$ of the hole left in the occupied valence bands (Kevan, 1992). Interaction effects, including for instance electron-phonon coupling, cause the infinitely sharp line spectrum of independent electron theory, $A_0(\mathbf{k}, \omega)$ = Im $G_0(\mathbf{k}, \omega)$ = Im $1/(\omega - \epsilon_{\mathbf{k}0} - i\eta)$, where $\epsilon_{\mathbf{k}0}$ represents a bare band dispersion, to evolve into Im $1/[\omega - \epsilon_{\mathbf{k}0} - \Sigma(\mathbf{k}, \omega)]$ where the complex self-energy $\Sigma(\mathbf{k}, \omega)$ contains the effects of the many body interactions. The spectral function of the photo-hole, $A(\mathbf{k}, \omega)$, then takes the form

$$A(\mathbf{k}, \omega) \propto \frac{\mathrm{Im}\Sigma(\mathbf{k}, \omega)}{[\omega - \epsilon_{\mathbf{k}0} - \mathrm{Re}\Sigma(\mathbf{k}, \omega)]^2 + (\mathrm{Im}\Sigma(\mathbf{k}, \omega))^2} \tag{1}$$

The real part, $\mathrm{Re}\Sigma(\mathbf{k}, \omega)$, gives a shift in energy and associated mass enhancement, while the imaginary part $\mathrm{Im}\Sigma(\mathbf{k}, \omega)$ gives the lifetime broadening of a quasiparticle. The spectral function $A(\mathbf{k}, \omega)$ is a fundamental quantity that determines all the properties of a many-body system. It can be directly measured in a photoemission experiment because the intensity of photoelectrons is given by $I(\mathbf{k}, \omega) = |M|^2 A(\mathbf{k}, \omega) f(\omega)$ where M represents the matrix element linking the initial and final states in the photoemission process, $A(\mathbf{k}, \omega)$ is the single particle spectral function given in equation (2) and $f(\omega)$ is the Fermi function which enters because the photoemission process is restricted to excitation from occupied states.

2.1 Electron-phonon coupling in photoemission

We now focus on the electron-phonon coupling. The electron-phonon coupling contribution, $\Gamma_{e-ph} = 2\mathrm{Im}\Sigma_{e-ph}$, to the total scattering rate may be calculated via the Eliashberg equation such that (Mahan, 1990)

$$\Gamma_{e-ph}(\omega, T) = 2\pi\hbar \int_{-\infty}^{\infty} d\omega' \alpha^2 F(\omega') \left[2n(\omega') + f(\omega' + \omega) + f(\omega' - \omega)\right] \tag{2}$$

where $\alpha^2 F$ is the Eliashberg function and $f(\omega)$ and $n(\omega)$ are the Fermi and Bose-Einstein distribution functions, respectively. (Grimvall, 1981) $\Gamma_{e-ph}(\omega, T)$ monotonically increases with energy over the region $|\omega| < \omega_{max}$ (for T=0), where ω_{max} is the cutoff of the phonon spectrum. The exact functional form is slightly dependent on the phonon spectrum. The temperature dependence of Γ_{e-ph} is approximately linear at higher temperatures, with slope
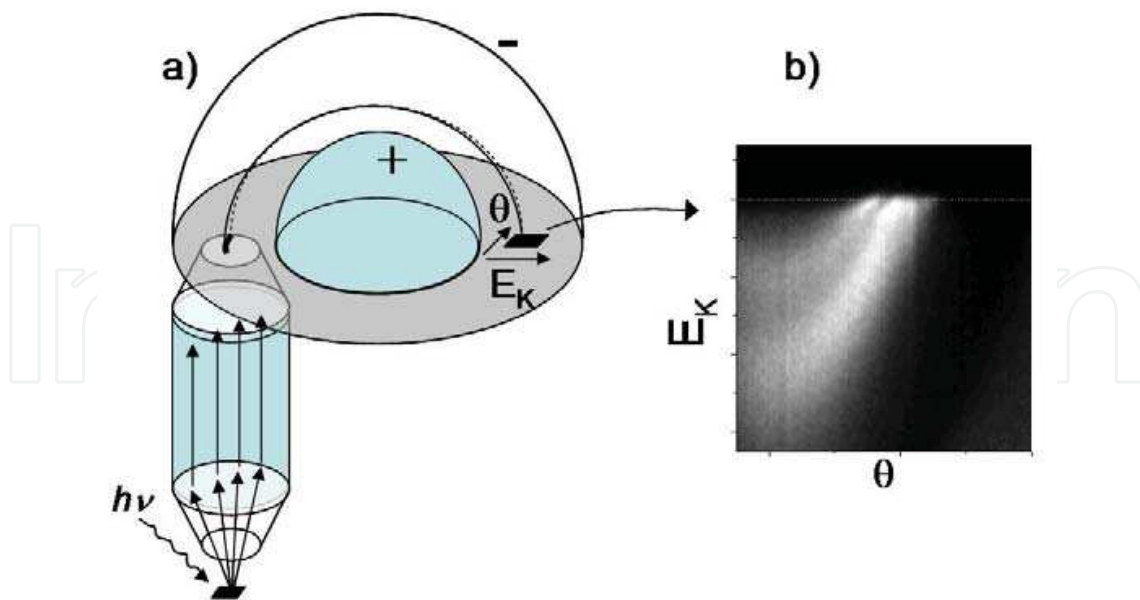
Fig. 1. Angle-resolved photoemission spectroscopy experiment. (a) Scienta hemispherical analyzer composes of a cylindrical lens, a hemispherical energy analyzer and a 2-dimensional detector (dark square). The entrance slit of the hemisphere selects a single angular line out of a finite solid angle collected by the lens. This defines a line in the inverse space over which the photoemission intensity is detected on a detector (b) Typical 2-dimensional photoemission intensity map as a function of kinetic energy E_K and angle θ from $NbSe_2$ sample (Valla et al., 2004). Bright (dark) represents high (low) photo-electron intensity.

$2\pi\lambda k_B$, where λ is the electron-phonon coupling constant given by (Grimvall, 1981)

$$\lambda = 2 \int\limits_0^\infty \frac{\alpha^2 F(\omega')}{\omega'} d\omega' \tag{3}$$

and k_B is Bolzman constant.

For most metals 10 meV $< \omega_{max} <$ 100 meV, and λ falls between 0.1 and 1.5. The electron-phonon coupling constant λ can be extracted directly from ReΣ as $\lambda = -[\partial(\text{Re}\Sigma)/\partial\omega]_0$ by fitting the low energy part of ReΣ to a straight line. The scattering process is illustrated in Fig. 2 where we consider a coupling to a single phonon mode at energy Ω_0. Coupling to such a mode (at T = 0 K) will result in a step function in the scattering rate or ImΣ. The step function reflects the observation that when the photohole has enough energy to create the mode ($\omega \geq \Omega_0$), scattering from the mode opens up a decay channel, thereby limiting the lifetime. The real and imaginary parts of the self energy are related via causality through a Kramers Kronig transform. Thus the step function in ImΣ results in a cusp function for ReΣ. Such an energy dependence of Σ affects the measured spectra in two ways. Above and below the mode energy there will be a noticeable change in the quasiparticle width. Secondly, the measured dispersion will be given by $\epsilon_{k0} + \text{Re}\Sigma(\mathbf{k},\omega)$ and will display the mass enhancement observed immediately below the Fermi level as presented in Fig. 2(e).

Modern photoelectron spectrometers allow the simultaneous measurement of photoelectron intensities from a finite range in both energy and momentum space. A typical image is shown in Fig. 1. The ability to obtain such images has led to the development of new methodologies for the extraction of self-energies. The spectral response in Fig. 1(b) may be analysed by taking
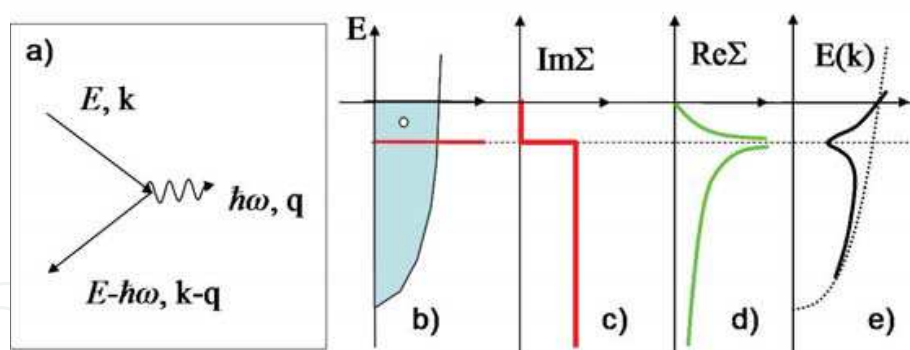
Fig. 2. Electron-phonon scattering (a) A Feynman diagram for the electron-phonon scattering. The straight lines represent the photo-hole states before and after scattering on a phonon (wiggly line). (b) The photo-hole created in photoemission (hollow circle) can emit a phonon only if it has enough energy. The red horizontal line indicates the energy of a phonon mode. (c) Imaginary part, $\text{Im}\Sigma$ of the self-energy. The step function reflects the opening of a decay channel when the photohole has enough energy to create the mode ($\omega \geq \Omega_0$). (d) Real part, $\text{Re}\Sigma$ of the self-energy. (e) The renormalized (observed) dispersion (thick solid line) is then obtained as a superposition of the bare dispersion (dotted line) and $\text{Re}\Sigma$.

an intensity cut at constant angle or momentum, the so called energy distribution curve or by taking an intensity cut at constant energy, a momentum distribution curve. In the limit of a momentum independent self-energy and a linear bare dispersion ($\epsilon_{k0} = v_0(k - k_F)$, where v_0 represents the bare velocity), the momentum distribution curve is a simple Lorentzian, centered at $k_m = k_F + [\omega_0 - \text{Re}\Sigma(\omega_0)]/v_0$ and with the full width at half maximum $\Delta k = 2\text{Im}\Sigma(\omega_0)/v_0$. The self-energy can thus be simply extracted from momentum distribution curve peaks at any binding energy, as has been discussed in several papers. (Kaminski et al., 2000; Kordyuk et al., 2005; LaShell et al., 2000; Valla et al., 2000) The same method of analysis has been employed here to study the electron-phonon coupling in GICs.

3. Photoemission from graphite intercalation compounds

The experiments were carried out on a Scienta SES-100 electron spectrometer operating in the angle resolved mode at the beamline 12.0.1 of the Advanced Light Source. The spectra were recorded at the photon energy of 50 eV with the combined instrumental energy resolution of 20-25 meV and the momentum resolution of 0.008 Å^{-1} in geometry where the polarization of light was perpendicular to the probed momentum line. The thin flake of pristine graphite was obtained by micromechanical exfoliation of HOPG on a SiO$_2$/Si substrate in air. From the optical contrast and from Raman data, the thickness of the flake was determined to be in the range of 7-9 graphene layers. The flake was annealed to 600 K in the ultra-high vacuum chamber before angle resolved photoemission studies. The LiC$_6$ and KC$_8$ samples were prepared by intercalating natural, single-crystal graphite flakes (Madagascan) as described in Ref. (Dresselhaus & Dresselhaus, 2002; Pruvost et al., 2004). The CaC$_6$ samples were prepared via immersion of a HOPG platelet or single-crystal graphite flake in a lithium/calcium alloy for 10 days. X-ray diffraction showed very high sample purity with no graphite or secondary stage phases. SQUID magnetometry revealed a sharp ($\Delta T \sim 0.3$K) superconducting transition at $\sim$ 11.6 K (onset) for CaC$_6$ samples. To avoid degradation, all samples were unsealed and glued to the sample holder with Ag- epoxy in an Ar filled glow box. Protected by the cured epoxy, they were then quickly transferred to the angle resolve photoemission prep-chamber,

and cleaved at low temperature (15-20 K) under ultra-high vacuum conditions (2×10^{-9} Pa). All data were collected at 15-20 K.

3.1 Electronic structure and charge transfer

Fig. 3 shows the angle resolved photoemission spectra near the K point in the graphene Brillouin zone for pristine graphite, LiC_6, KC_8 and CaC_6. The upper panels (a) - (d) show the contours of photoemission intensity as a function of binding energy for a momentum line going through the K point. The intensity from a narrow interval (± 10 meV) around the Fermi level, representing the Fermi surface, is shown in the lower panels (e) - (h). The dispersing states are the graphene-derived π and π^* bands, as marked in Fig. 3(a) through (d). In KC_8 the low energy band structure is essentially graphene-like, with π and π^* bands touching at the Dirac point (Grüneis et al., 2009), shifted below the Fermi level due to the electron doping. In LiC_6 and CaC_6 a sizable gap exists between π and π^* bands. Dirac point is determined
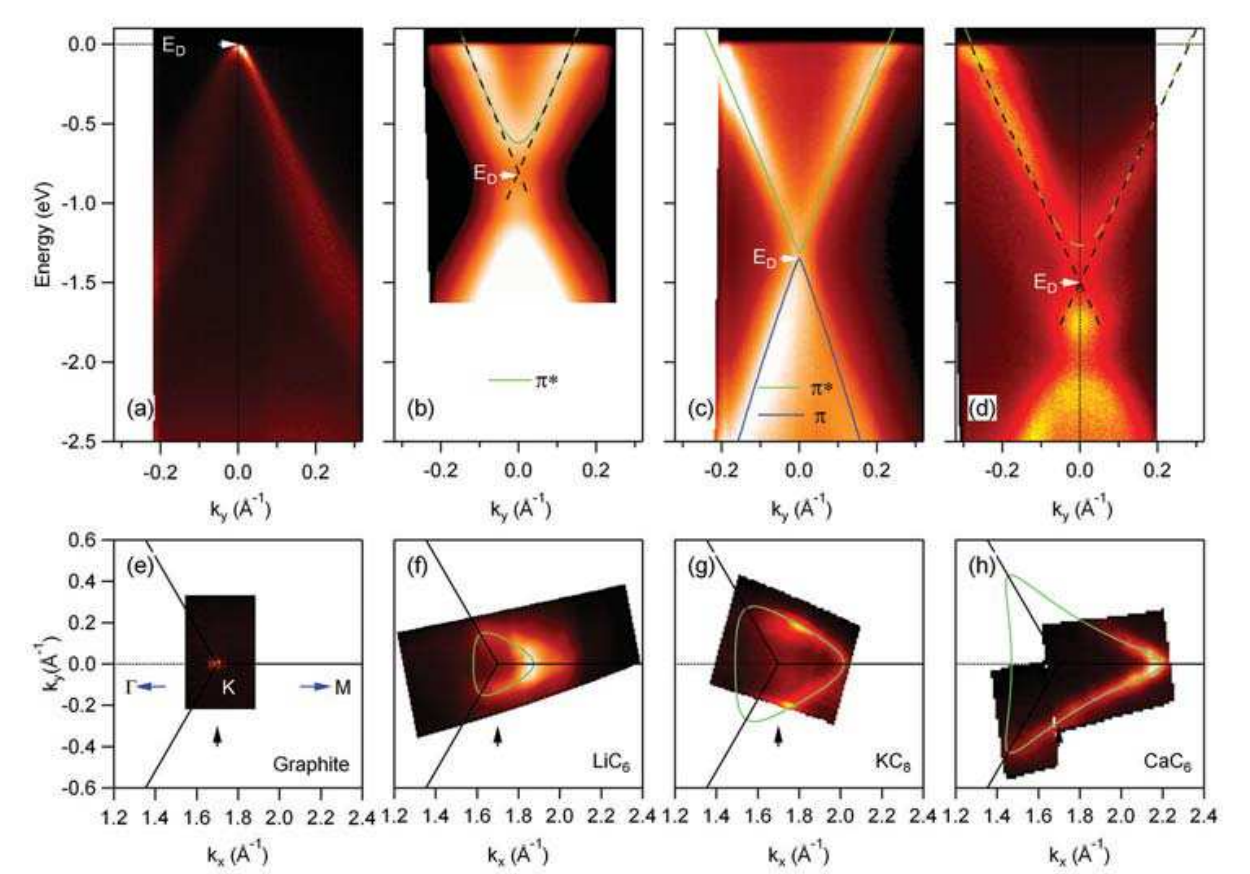

Fig. 3. Photoemission from pristine and intercalated graphite. Photoemission spectra from pristine graphite (a), LiC_6 (b), KC_8 (c) and CaC_6 (d) along the same momentum line in the graphene Brillouin Zone traversing the K point, as indicated by the black arrows in panels (e)-(h). Blue and green lines represent the π and π^* bands. White arrows indicate position of Dirac point. (e)-(h) Photoemission intensity from a narrow energy interval around the Fermi level ($\omega = \pm 10$ meV), representing the graphene-derived π^* Fermi surface, for graphite, LiC_6, KC_8 and CaC_6 respectively. The green lines represent tight-binding fits to the Fermi surface. All spectra were taken at T ~ 15 K.

by extrapolating the linear part of π^* dispersion at low binding energies to the K point. The arrows indicate positions of Dirac point, (E_D), 0 eV, 0.825 eV, 1.35 eV and 1.5eV for pristine

graphite, LiC_6, KC_8 and CaC_6, respectively, indicating that the filling of the π^* band increases in that sequence. In particular, it appears that the π^* band is filled more in KC_8 than in LiC_6 and that it forms a larger Fermi surface in the former material. The area enclosed by the Fermi surface (lower panels in Fig. 3) is a direct measure of doping of graphene π^* states, i.e. of the charge transferred into the graphene sheets. The Fermi surface area is determined from peak positions of momentum distribution curves at Fermi level and compared to the 3rd nearest neighbor hopping tight binding band structure. In pristine graphite, the Fermi surface is essentially a point, indicating nearly neutral graphene sheets. In the intercalated samples the Fermi surface grows from LiC_6 to KC_8 to CaC_6. Its area is 0.399 Å^{-2} in KC_8, corresponding to 0.11 electrons per graphene unit cell, or 44% of the nominal value of 0.25 for the complete charge transfer. In LiC_6, the enclosed area is 0.125 Å^{-2}, corresponding to the doping of only 0.0344 electrons per graphene unit cell (GUC). This is far below the nominal value of 1/3 electrons per graphite unit cell expected for the complete intercalant ionization. For CaC_6 the complete charge transfer would involve a donation of 2 calcium electrons to the graphene sheets, equivalent of the doping of 1/3 electrons per C atom (or $2/3e^-$ per unit cell). Instead, the measured Fermi area gives approximately 0.18 electrons per C atom.

The incomplete charge transfer into the graphene π^* states would suggest that the remaining charge occupies the so-called interlayer band. There has been a substantial body of theoretical work that depicts the intercalant-derived interlayer states and phonons as main contributors to superconductivity in GICs. However, so far there has been no clear evidence of the intercalant-derived nearly free electron band in photoemission experiments. The occupation of the interlayer state has been recently reported in CaC_6 (Sugawara et al., 2008), but the observed feature was very weak and broad. There, even the graphene-derived π^* state was very broad and did not form an enclosed contour at the Fermi level, casting doubts on these results. Our experiments always show relatively sharp π^* band that forms a well defined Fermi surface. However, in MC_6(M=Li, Ca, Ba) materials, in addition to π^* band, we always see a broad feature at slightly higher binding energy that follows the π^* band, dispersing upward from K point (Fig. 3(b)and (d)). Further from the K point, it loses intensity and its dispersion cannot be precisely traced. In CaC_6, this feature is observable over larger region of k space (Valla et al., 2009). It is possible that this is a remnant of an interlayer band, smeared out by a disorder within the intercalant layers and folded into the K point of the graphene Brillouin zone. However, our measurements do not show any evidence of the interlayer band in the region from which it should be folded to the K point - the Γ point. Of course, the missing charge has to be somewhere and even if the state is completely incoherent it still can count for the missing charge. We note that in pristine graphite, the interlayer hopping $t_\perp$ splits both π and π^* bands into the bonding and antibonding counterparts due to the AB stacking of graphene sheets. It would be tempting to assign the broad feature to a bonding π^* state, due to similarities with π^* in initial dispersion. However, unlike the pristine graphite, all the first stage GICs have the AA stacking of graphene sheets and such assignment would be incorrect. On the other hand, in LiC_6 and CaC_6 the π^* band might be split due to the AB stacking of the intercalant (if there is not too much disorder in the intercalant sites). If this was indeed the case, we counted only a portion of charge transferred to graphene layers. The alternative charge counts would be in this case 0.0616 and 0.349 electrons per C atom, for LiC_6 and for CaC_6, respectively. We point out that, if this is indeed the case, only the antibonding counterpart, which appears more coherent, plays a significant role in superconductivity, because it is its filling and its coupling to phonons that determines T_c, as will be shown in the next section. Irrespective of these issues, our experimental observation that the doping of graphene sheets is larger in KC_8 than in LiC_6 is opposite of the expected nominal doping, but is in line with the existence of superconductivity in these materials: KC_8 is a superconductor and LiC_6 is

not. In the following, we identify the reason for the correlation between superconductivity and doping of the graphene sheets.

3.2 Electron-Phonon Coupling in Graphite Intercalation Compounds

It is evident from Fig. 3 that in all three intercalated materials, an anomaly or a kink in dispersion of the π^* band occurs at approximately 160 meV below the Fermi level. This is a hallmark of the interaction of the electronic states with phonons (Hengsberger et al., 1999; Valla et al., 1999) that has been attributed to a coupling to graphene in- plane high-frequency phonons(Grüneis et al., 2009; Pan et al., 2010; Valla et al., 2009). We now focus on CaC_6, a system in which these effects are the most pronounced. Fig. 4 shows the angle resolved
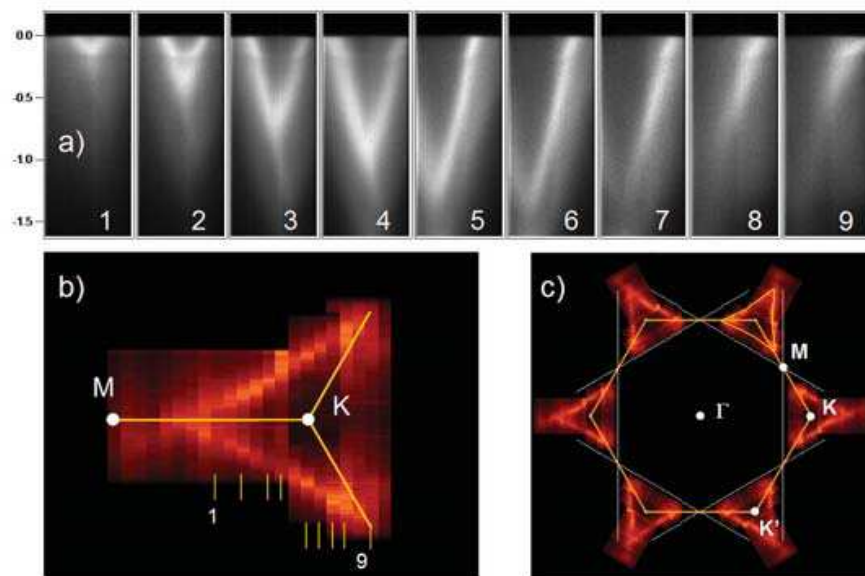
Fig. 4. Photoemission from CaC_6. (a) 1-9: photoemission spectra from CaC_6 along several momentum lines near the K point as indicated in (b). (b) Photoemission intensity from CaC_6 from a narrow energy interval around the Fermi level ($\omega = \pm10$ meV) near the K point of the graphene Brillouin zone. Thin bars indicate momentum lines probed in (a). (c) Fermi surface of CaC_6 obtained by six fold symmetrization of intensity shown in (b). White lines correspond to the doping of 0.5 electrons per C atom, at which the van Hove singularity in the π^* band sits at the Fermi level.

photoemission spectra near the K point in the graphene Brillouin zone. The upper panel (a) shows the contours of photoemission intensity as a function of binding energy for several momentum lines in the vicinity of K point, while the intensity from a narrow interval (±10 meV) around the Fermi level is shown in the lower contours (b and c). All the spectra are shown on the same momentum and energy scales and all were taken in the normal state, at T=15 K. The Fermi surface of CaC_6 encloses a significant area and has a concave triangular shape centred at the K point of the Brillouin zone. The charge transfer from intercalant atoms fills the graphene bands and the Dirac point has moved to 1.5 eV below the Fermi level. White lines in Fig. 4c) correspond to the doping of 0.5 electrons per C atom, at which the van Hove singularity in the π^* band sits at the Fermi level. An important observation can immediately be made: in all the spectra from Fig. 4a), there is a renormalization of the quasiparticle dispersion at $\sim$160 meV below the Fermi level.
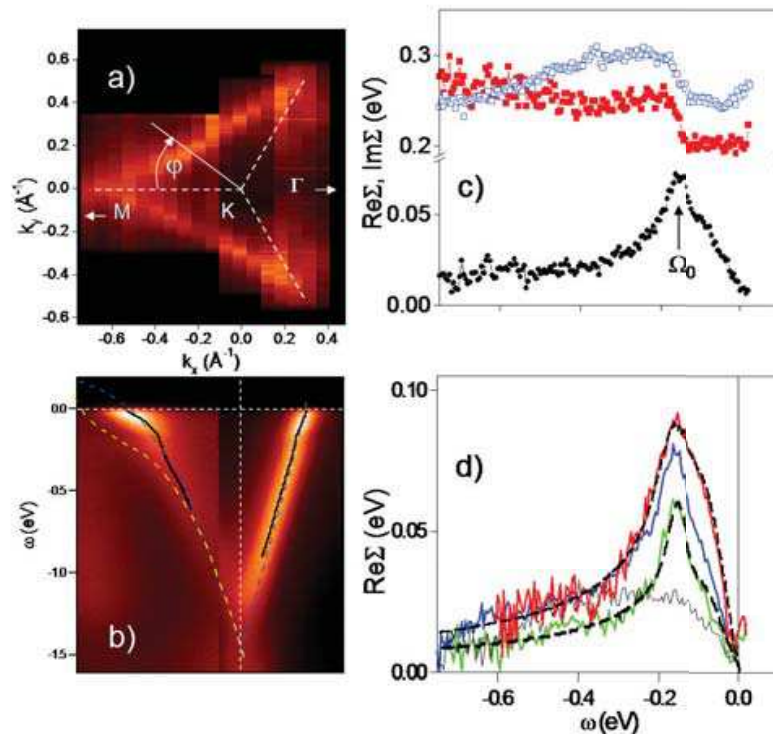
Fig. 5. Electron-phonon coupling in CaC_6. (a) Fermi surface of CaC_6. ϕ defines the polar angle around the K point, measured from the KM line. (b) Spectral intensity for $\phi = 60°$ or $K\Gamma$ line (right) and $\phi = 0°$ or KM line (left). Black solid lines represent the momentum distribution curve derived dispersions. Dashed blue and yellow lines represent bands from Ref. (Calandra & Mauri, 2007), calculated for graphene and CaC_6 monolayer, respectively. (c) $Re\Sigma$ (black circles) and $Im\Sigma$ (red solid squares) for $\phi = 43°$ and $Im\Sigma$ for $\phi = 35°$ (blue open squares). Peak (step) position in $Re\Sigma$ ($Im\Sigma$) is labeled with Ω_0. (d) Real part of the self-energy for $\phi = 53°, 32°$ and $2°$ (bottom to top). Dashed lines represent the fits to the simple model self-energies as described in text. Thin black line is $Re\Sigma$ of pristine graphite flake.

It is also apparent from Fig. 4 that the renormalization effects ("kinks") are not equally strong for all the points on the Fermi surface. Fig. 5 illustrates the anisotropy of the renormalization effects in CaC_6. We have extracted the dispersions and the linewidths of the quasiparticle states by fitting the spectral intensities at constant energies, or momentum distribution curves (Valla et al., 1999), with Lorentzian distributions. The real and imaginary components of the self-energy are then derived in the usual manner from the peak positions k_m and widths Δk of the momentum distribution curve peaks at each ω, as described in section 2.1, using the expressions

$$\mathrm{Re}\Sigma(\omega) = (k_m - k_0)v_0(\omega), \quad \mathrm{Im}\Sigma(\omega) = \frac{\Delta k}{2}v_0(\omega) \tag{4}$$

where v_0 represents the bare band velocity at ω (LaShell et al., 2000; Valla et al., 2000). The starting approximation for the bare band was a tight binding dispersion which was then refined until the obtained $Re\Sigma$ and $Im\Sigma$ satisfied Kramers-Kronig transformations (Kordyuk et al., 2005). We note that the choice of the bare dispersion may play a significant role in determining the exact shape and magnitude of the self-energy (Valla et al., 2000). Therefore, the self-consistency check through the Kramers-Kronig criterion is important in getting the correct results. We note that the bands calculated for a CaC_6 monolayer (dashed blue line

in Fig. 5(b) (Calandra & Mauri, 2007) do not realistically represent the bare dispersions in our case. Instead, we have found that the bare dispersions calculated within 3rd nearest neighbor tight binding approximation and appropriately filled, work well for the whole Fermi surface. The results for ReΣ and ImΣ corresponding to the azimuthal angle $\phi = 43°$ and ImΣ for $\phi = 35°$ are shown in Fig. 5(c). Fig. 5(d) shows ReΣ for different momentum lines corresponding, from bottom to top, to azimuthal angles $\phi = 53°$, $32°$ and $2°$. All the self-energies have a structure typical for the interaction with a well defined bosonic mode: the imaginary part has a sharp step-like feature, while the real part has a peak at the energy of the mode, Ω_0. Therefore, the mode energy can be read directly from the measured self-energy. In our case, the dominant structure occurs at $\sim$160 meV, with an additional feature at $\sim$75 meV. These features can be naturally attributed to the interaction with in-plane and out-of-plane phonons of the graphene sheets. We note that the finite energy resolution also affects the measured ReΣ near the Fermi level, within the resolution range, but with the tendency to underestimate the measured electron-phonon coupling (Valla, 2006). We have excluded the affected interval $|\omega| < 20$ meV from the considerations and any fine structure, related to a possible coupling to the intercalant modes, is out of our detection limits. At higher energies, we can model the measured self-energy at any ϕ with an Eliashberg function, $\alpha^2 F(\omega)$ (see equation 2), consisting of two peaks: one fixed at 75 meV and the other ranging from 155 to 165 meV. The relative contribution of these two peaks increases from 1:5 to almost 1:1 on moving from $\phi = 60°$ to $\phi = 0$. The modelled ReΣ are shown for these two limiting cases. Our model assumes a constant density of states (DOS), whereas a linear DOS would be a better approximation since the scattering is expected to reflect the density of final states. This is visible in Fig. 5(c), where ImΣ quickly acquires a slope as one moves from ΓK to KM. Fitting of measured ReΣ in the energy range $20 \leq |\omega| \leq 300$ meV to the model gives the energy of the high frequency mode Ω_0. In addition, the coupling strength, λ, can be extracted from the low energy slope of ReΣ, $\lambda = -[\partial(\text{Re}\Sigma)/\partial\omega]_0$ by fitting the low energy part of ReΣ to a straight line. From Fig. 5(d) it is clear that the characteristic energy Ω_0 does not vary a lot, whereas the coupling strength λ displays a significant anisotropy. In Fig. 6(e-f), we plot both quantities as functions of azimuthal angle ϕ. The coupling constant ranges from 0.38 (for $\phi \approx 60°$) to 0.89 (for $\phi \approx 0$), with the momentum averaged value of 0.53. The coupling constant in pristine graphite flake is much smaller ($\lambda = 0.16$) and does not show a significant anisotropy, in agreement with Leem et al. (Leem et al., 2008). The measured Fermi velocity on the graphene-derived Fermi surface is also very anisotropic: $v_F(\phi = 0) \approx 1.1$ eVÅ, $v_F(\phi = 60°) \approx 4.1$eVÅ, with the momentum average $\langle v_F(k) \rangle \approx 2.5$ eVÅ. If the graphene electrons were responsible for superconducting properties, the in-plane coherence length, $\epsilon_{ab} = v_F/(\pi\Delta)$, would be in the range 200Å$< \epsilon_{ab} < 800$ Å, if we take $\Delta \approx 1.6$ meV for the superconducting gap (Bergeal et al., 2006). $\langle v_F(k) \rangle$ gives $\epsilon_{ab} \approx$500 Å, in reasonable agreement with $\epsilon_{ab} \approx$350 Å reported in scanning tunneling microscopy (Park et al., 2007), specific heat (Kim et al., 2006) and magnetization (Emery et al., 2005; Lamura et al., 2006) studies. We also note that peculiar linearity in the upper critical filed, H$_{C2}$, at low temperatures, could also be explained by anisotropic Fermi velocity on the graphene-derived Fermi surface (Mazin et al., 2007). In contrast, the highly isotropic intercalant Fermi surface would not produce linear H$_{C2}$. Recent theoretical calculations suggest that in CaC$_6$, the crucial role is played by calcium, i.e. electrons on the intercalant-derived Fermi surface are strongly coupled to the intercalant vibrations (Boeri et al., 2007; Calandra & Mauri, 2005; Csányi et al., 2005; Mazin, 2005). Those calculations show nearly one order of magnitude weaker coupling of the graphene-derived electrons to the in-plane graphene phonons, with essentially no anisotropy (Park et al., 2008). The large calcium isotope effect also implies the dominant role of soft Ca vibrations

in superconductivity (Hinks et al., 2007). Our results, on the contrary, suggest that graphene sheets play the dominant role because the obtained electron-phonon coupling on graphene-derived Fermi surface with the in-plane and out-of-plane graphene phonons seems to be more than sufficient to give $T_c \sim 11.6$ K in CaC_6.
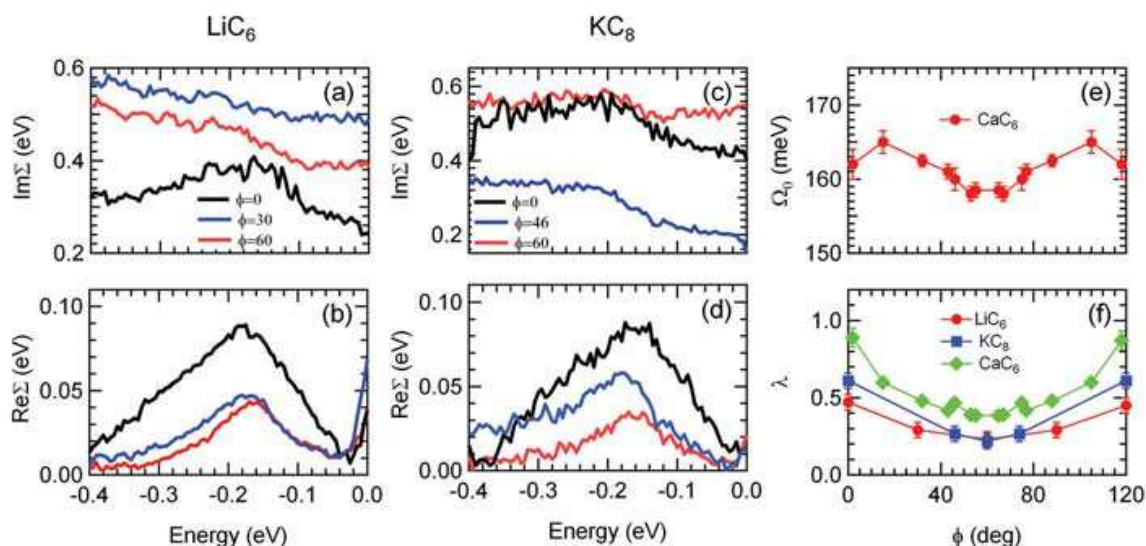

Fig. 6. Self-energy and electron-phonon coupling in graphite intercalation compouds. $Im\Sigma(\omega)$ (a) and $Re\Sigma(\omega)$ (b) for LiC_6 and KC_8 ((c) and (d)) for several different points at the Fermi surface as indicated by the polar angle ϕ. (e) Characteristic energy Ω_0 of the maximum in $Re\Sigma(\omega)$ of CaC_6 as a function of ϕ. (f) The electron phonon coupling constant λ in LiC_6, KC_8 and CaC_6, extracted from $Re\Sigma$ as a function of ϕ.

By extending similar analysis to a whole series of graphite intercalation compounds, including LiC_6, KC_8, KC_{24} (Camacho et al., n.d.; Pan et al., 2010), and BaC_6, we have been able to track certain trends and to get a better insight into the mechanism of superconductivity in the intercalated graphite. Fig. 6 shows the self-energies and the extracted electron-phonon coupling for the two most interesting members of the series: LiC_6, KC_8. The superconducting transition temperature, T_c, in these two materials is inverted from the expected trend in which the more charge nominally transferred to graphene sheets would mean the higher T_c. However, the actual charge transfer to graphene sheets measured in photoemission, is different from the nominal one dictated by the chemical formula (see Fig. 3) and, as previously discussed, it is actually larger in KC_8 than in LiC_6. Following the same procedure as for CaC_6, we have extracted the electron-phonon coupling from the self-energies. The coupling in both materials shows some anisotropy [Fig. 6(f)], with the maximum along the KM direction and the minimum along the ΓK direction, similar, but significantly weaker than in CaC_6(Valla et al., 2009) and what was recently reported for KC_8 (Grüneis et al., 2009). The most important observation, however, is that the momentum averaged $\langle\lambda_k\rangle$ is stronger in KC_8 than in LiC_6. The coupling constant and its anisotropy both increase from LiC_6 to KC_8 to CaC_6, exactly in the same sequence as the actual filling of the graphene π^* band and in previously established sequence for T_c. Strengthening of the electron-phonon coupling with the filling of the π^* band has also been observed in the epitaxial graphene (McChesney et al., 2007). This is not surprising, because the density of states near the Fermi level increases with the filling of the π^* band. Also, a larger Fermi surface makes an electron-phonon scattering process more probable as the phase space available for the scattering events grows. In the pristine graphite, the Fermi surface is nearly a point and the coupling is strongly suppressed (Leem et al.,
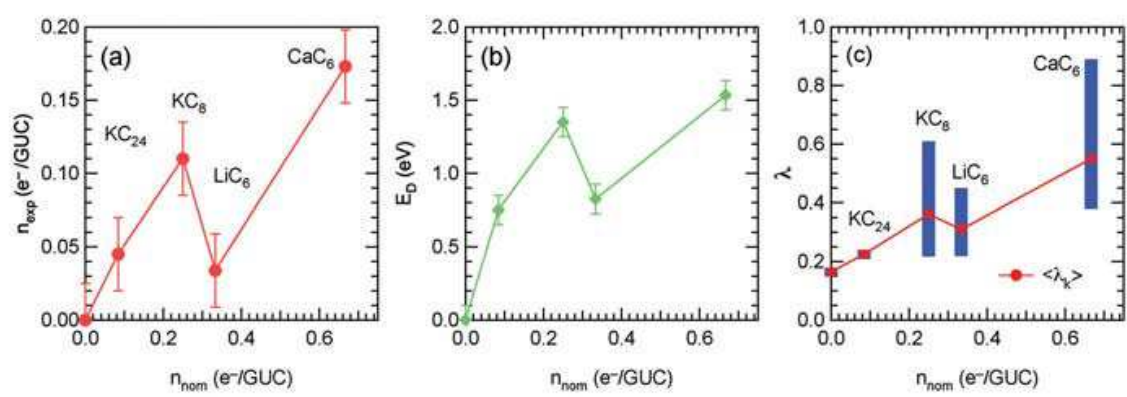
Fig. 7. Electron-phonon coupling and the filling of graphene states. (a) Measured charge transfer from the intercalant to the graphite π^* states. (b) Binding energy of Dirac point (chemical potential shift). (c) electron-phonon coupling, λ. The range of each vertical bar indicates the anisotropy with the maximum along the K-M line and minimum along the K-Γ line. Red circles represent the momentum averaged values, $\langle \lambda_k \rangle$.

2008; Valla et al., 2009). To better illustrate the positive correlation between the filling of the graphene π^* band and the coupling strength λ in different GICs, we plot these quantities in Fig. 7 as functions of nominal chemical composition for several different materials. The actual (measured) charge transfer (in electrons/GUC), obtained fom the Fermi surface area, is shown in Fig. 7(a). The increase in size of the Fermi surface is consistent with the energy of Dirac point [panel (b)] as the chemical potential, μ, shifts from the pristine graphite to CaC$_6$. It is interesting to note that $\mu \propto \sqrt{n}_{exp}$ still holds, regardless of the shape of Fermi surface and number of Fermi sheets in these five different materials. The coupling constant λ [panel (c)] follows the same trend as the filling of the π^* band. Note that this is the very trend of superconducting transition temperatures (T_c) in these materials, plotted in Fig. 8(c). This correlation suggests that the graphene π^* states and their coupling to graphene in-plane phonons is crucial for superconductivity in graphite intercalation compounds. The only role that the intercalants seem to play is to provide the charge for filling of the π^* states. As an additional test of this idea we have calculated the superconducting transition temperature, T_c, from McMillan's formula (McMillan, 1968), using the measured coupling constants $\langle \lambda_k \rangle$ and Coulomb pseudo-potential $\mu^* = 0.14$. The calculated T_c is compared with the experimental one in Fig. 8(b-c). It is clear not only that the calculated T_c follows the same trend, but even the absolute values are very close to the measured ones. This reinforces our conclusion that the graphene electronic states and graphene-derived phonons are crucial for superconductivity in GICs. Note that the threshold-like behavior near $\langle \lambda_k \rangle = 0.3$ places LiC$_6$ on one side and KC$_8$ on another side of a steep increase in T_c. We note that superconductivity in LiC$_3$ and LiC$_2$, materials in which more Li is pushed in under pressure, supports our picture where the electron-phonon coupling and superconductivity strengthen with the filling of graphene π^* states. The increase in T_c from 0.39 K for stoichiometric KC$_8$ to 0.55K in material with excess K is also in line with this picture. A further test would be a systematic photoemission study on alkaline-earth GICs (Ca, Sr, Ba) where T_c decreases with the atomic mass of alkaline-earth intercalant.
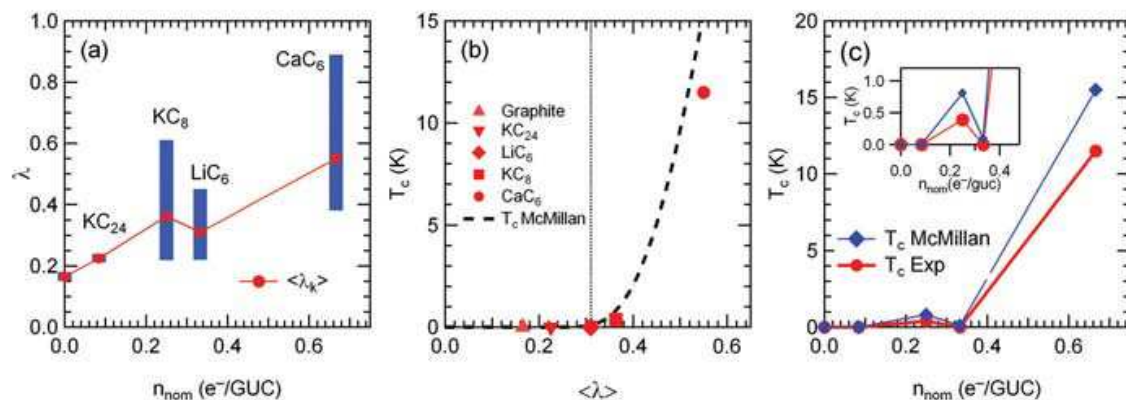
Fig. 8. Electron-phonon coupling and superconducting critical temperature (T_c) in graphite intercalation compunds. (a) Measured λ for several different GICs. The range of each vertical bar indicates the anisotropy with the maximum along the KM line and minimum along the KΓ line. The red circles and line represent the momentum averaged values $\langle \lambda_k \rangle$. (b) T_c as a function of $\langle \lambda_k \rangle$ calculated from measured $\langle \lambda_k \rangle$ using McMillan's formula (McMillan, 1968). The dashed line represents the calculated values while symbols represent experimental T_c values. (c) Comparison of calculated (blue diamond) and measured (red circle) values as functions of nominal chemical composition (electrons per graphene unit cell (GUC)) for measured GICs. Zero corresponds to the pristine graphite. The inset zooms in the low T_c values.

3.3 Enhancement of electron-phonon coupling via dynamical nesting

A huge discrepancy between the calculated and measured coupling, where the later one is almost one order of magnitude stronger, naturally provokes the question: Where is such strong and anisotropic coupling coming from? Similar anisotropy was recently reported for electron-phonon coupling in K and Ca doped graphene on SiC (McChesney et al., 2007). There, the proximity of van Hove singularity to the Fermi level was suggested to be an origin of the enhanced coupling. Even though the claim on very high anisotropy was subsequently retracted due to the erroneous procedure of extracting the coupling near the KM lines, the measured coupling on the unaffected portion of the Fermi surface was still significantly stronger than the calculated one (Park et al., 2008). In the case of CaC_6 we believe that we have found the likely mechanism of enhancement of the coupling: very favourable dynamical nesting conditions exist on the Fermi surface that may strongly enhance the inter-valley coupling.

This is illustrated in Fig. 9. In order to satisfy the energy conservation rule in an electron-phonon scattering event, the photohole created at ~ 160 meV has to be scattered to the Fermi level after emission of a 160 meV phonon. To explore the allowed momenta in such a process, we plot the states at $\omega = -160$ meV at one corner of the Brillouin zone and the states at the Fermi level ($\omega = 0$) in another corner for two highly doped GICs: KC_8 (panel (a)) and CaC_6 (panel (b)). A wavevector connecting any pair of points on different contours represents an allowed scattering process. Note that in the case of intra-valley scattering, both contours would have to be centred at the same K point. However, from the measured phonon spectra in graphite (Maultzsch et al., 2004), and recent Raman experiments on CaC_6 (Hlinka et al., 2007), it is clear that there are no $q \approx 0$ modes at ~ 160 meV and we have to consider inter-valley scattering.
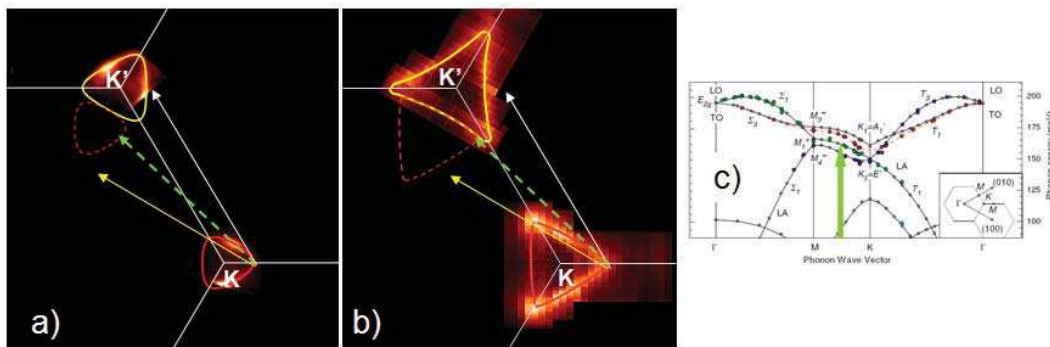
Fig. 9. Dynamical nesting of the Fermi surface in GICs. Contour of photoemission intensity from KC_8 (a) and CaC_6 (b) at $\omega = 0$ meV (yellow contour) around K' point and at the "kink" energy $\omega = -\Omega_0 = -160$ meV (red contour), in the vicinity of of K point of the Brillouin zone. White (yellow) arrow represents the ΓK (ΓM) wave vector, while the dashed green arrow represents the wave vector that "nests" the two contours. Evidently, the nesting is much more efficient in CaC_6 than in KC_8. (c) Phonon dispersions in pristine graphite (Maultzsch et al., 2004). The position of dynamical nesting wave vector for CaC_6 from(b) is marked with green arrow. Its length corresponds to the exchanged energy.

From Fig. 9, it appears that in the case of CaC_6, some wave-vectors are particularly efficient in connecting the two contours. As the $\omega = -160$ meV contour is slightly convex and the Fermi surface is slightly concave with essentially the same curvature, the green vector in Fig 9(b) effectively nests the whole side, or $\sim$ 1/3 of the length of the two contours. The tips of contours can be nested by two such vectors, which might explain a portion of the observed anisotropy in λ. The additional factor characterizing the tips is a gain in coupling to lower frequency phonons at $\omega \approx 75$ meV, as can be seen in Fig. 5d. We note that the observed "nesting" is not static: it involves emission/absorption of a high frequency phonon and would not produce the charge density wave instability. The dynamical nesting and resulting enhancement of the electron-phonon coupling is obviously very sensitive to the filling of graphene-derived bands. For lower doping levels, the nesting efficiency is quickly lost as both contours become convex, as is evident in the case of KC_8 (Fig. 9(a)). At even higher fillings, possibly realized under pressure (Gauzzi et al., 2007; Smith et al., 2006), the nesting conditions would likely improve further, but at some point, the coupling to lower frequency phonons near the KM lines might become too strong and eventually drive the system into the charge-density wave state.

4. Summary and outlook

In conclusion, we have performed angle resolved photoemission spectroscopy studies of the electronic structure in pristine graphite and several alkali and alkaline-earth GICs. We have measured the strength of the electron-phonon interaction on the graphene-derived Fermi surface to carbon derived phonons in these materials and found that it follows a universal trend where the coupling strength and superconductivity monotonically increase with transfer of electrons into the graphene-derived π^* states. This correlation between the filling of graphene π^* states, the strength of the electron-phonon coupling and superconductivity suggests that both graphene-derived electrons and graphene-derived phonons are crucial for superconductivity in GICs. We have also identified a possible mechanism of enhancement of the electron-phonon coupling in these materials that stems from the particular Fermi surface geometry. For highly doped systems (CaC_6), a concave triangular shape of the Fermi

surface perfectly matches the convex energy contour at the energy of the exchanged phonon, effectivley enhancing the electron-phonon coupling. Such mechanism is expected to be very sensitive on the occupation of the π^* band and might be used to fine-tune the coupling in order to reach a maximal T_c. Perhaps this is what is going on under pressure in some superconducting GICs (Gauzzi et al., 2007; Smith et al., 2006).

We note that similar results were obtained for graphene monolayers, epitaxially grown on SiC(0001) and Ir(111) and chemically doped by adsorbed (or subsurface) alkali and alkaline-earth atoms (Bianchi et al., 2010; McChesney et al., 2007; 2010). Due to the reduced dimensionality, we probably cannot expect these systems to be superconducting, but the ability to contionusly fill the π^* states and to fine tune the electronic structure in these films offers the opportunity of measuring the electron-phonon coupling in much finer steps of doping. Such studies might help in understanding the role of the Fermi surface topology in shaping the properties of graphite intercalation compounds and open the new avenues of designed synthesis of new intercalated materials with targeted properties.

5. Acknowledgments

## 6. References

Bergeal, N., Dubost, V., Noat, Y., Sacks, W., Roditchev, D., Emery, N., Hérold, C., Marêché, J.-F., Lagrange, P. & Loupias, G. (2006). Scanning tunneling spectroscopy on the novel superconductor CaC_6, *Phys. Rev. Lett.* 97(7): 077003.

Bianchi, M., Rienks, E. D. L., Lizzit, S., Baraldi, A., Balog, R., Hornekær, L. & Hofmann, P. (2010). Electron-phonon coupling in potassium-doped graphene: Angle-resolved photoemission spectroscopy, *Phys. Rev. B* 81(4): 041403.

Boeri, L., Bachelet, G. B., Giantomassi, M. & Andersen, O. K. (2007). Electron-phonon interaction in graphite intercalation compounds, *Phys. Rev. B* 76(6): 064510.

Calandra, M. & Mauri, F. (2005). Theoretical explanation of superconductivity in C_6Ca, *Phys. Rev. Lett.* 95(23): 237002.

Calandra, M. & Mauri, F. (2007). Electronic structure of heavily doped graphene: The role of foreign atom states, *Phys. Rev. B* 76(16): 161406.

Camacho, J., Upton, M., Pan, Z.-H., Howard, C., Ellerby, M. & Valla, T. (n.d.). unpublished.

Csányi, G., Littlewood, P. B., Nevidomskyy, A. H., Pickard, C. J. & Simons, B. D. (2005). The role of the interlayer state in the electronic structure of superconducting graphite intercalated compounds, *Nature Physics* 1(1): 42–45.
    URL: *http://www.nature.com/doifinder/10.1038/nphys119*

Dean, M. P. M., Howard, C. A., Saxena, S. S. & Ellerby, M. (2010). Nonadiabatic phonons within the doped graphene layers of XC_6 compounds, *Phys. Rev. B* 81(4): 045405.

Dresselhaus, M. S. & Dresselhaus, G. (2002). Intercalation compounds of graphite, *Advances in Physics* 51(1): 1–186.
    URL: *http://www.informaworld.com*

Emery, N., Hérold, C., d'Astuto, M., Garcia, V., Bellin, C., Marêché, J. F., Lagrange, P. & Loupias, G. (2005). Superconductivity of bulk CaC_6, *Phys. Rev. Lett.* 95(8): 087003.

Gauzzi, A., Takashima, S., Takeshita, N., Terakura, C., Takagi, H., Emery, N., Hérold, C., Lagrange, P. & Loupias, G. (2007). Enhancement of superconductivity and evidence of structural instability in intercalated graphite CaC_6 under high pressure, *Phys. Rev. Lett.* 98(6): 067002.

Grimvall, G. (1981). *The Electron-Phonon Interaction in Metals*, North-Holland, New York.

Grüneis, A., Attaccalite, C., Rubio, A., Vyalikh, D. V., Molodtsov, S. L., Fink, J., Follath, R., Eberhardt, W., Büchner, B. & Pichler, T. (2009). Angle-resolved photoemission study of the graphite intercalation compound KC_8 : A key to graphene, *Phys. Rev. B* 80(7): 075431.

Hannay, N. B., Geballe, T. H., Matthias, B. T., Andres, K., Schmidt, P. & MacNair, D. (1965). Superconductivity in graphitic compounds, *Phys. Rev. Lett.* 14(7): 225–226.

Hengsberger, M., Purdie, D., Segovia, P., Garnier, M. & Baer, Y. (1999). Photoemission study of a strongly coupled electron-phonon system, *Phys. Rev. Lett.* 83(3): 592–595.

Hinks, D. G., Rosenmann, D., Claus, H., Bailey, M. S. & Jorgensen, J. D. (2007). Large Ca isotope effect in the CaC_6 superconductor, *Phys. Rev. B* 75(1): 014509.

Hlinka, J., Gregora, I., Pokorny, J., Hérold, C., Emery, N., Marêché, J. F. & Lagrange, P. (2007). Lattice dynamics of CaC_6 by Raman spectroscopy, *Phys. Rev. B* 76(14): 144512.

Holzwarth, N. A. W., Louie, S. G. & Rabii, S. (1984). Interlayer states in graphite and in alkali-metal-graphite intercalation compounds, *Phys. Rev. B* 30(4): 2219–2222.

Kaminski, A., Mesot, J., Fretwell, H., Campuzano, J. C., Norman, M. R., Randeria, M., Ding, H., Sato, T., Takahashi, T., Mochiku, T., Kadowaki, K. & Hoechst, H. (2000). Quasiparticles in the superconducting state of $Bi_2Sr_2CaCu_2O_{8+\delta}$, *Phys. Rev. Lett.* 84(8): 1788–1791.

Kevan, E. (1992). *Angle-Resolved Photoemission*, Elsevier, Amsterdam.

Kim, J. S., Kremer, R. K., Boeri, L. & Razavi, F. S. (2006). Specific heat of the Ca-intercalated graphite superconductor CaC_6, *Phys. Rev. Lett.* 96(21): 217002.

Kordyuk, A. A., Borisenko, S. V., Koitzsch, A., Fink, J., Knupfer, M. & Berger, H. (2005). Bare electron dispersion from experiment: Self-consistent self-energy analysis of photoemission data, *Phys. Rev. B* 71(21): 214513.

Lamura, G., Aurino, M., Cifariello, G., Di Gennaro, E., Andreone, A., Emery, N., Hérold, C., Marêché, J.-F. & Lagrange, P. (2006). Experimental evidence of *s*-wave superconductivity in bulk CaC_6, *Phys. Rev. Lett.* 96(10): 107008.

LaShell, S., Jensen, E. & Balasubramanian, T. (2000). Nonquasiparticle structure in the photoemission spectra from the Be(0001) surface and determination of the electron self energy, *Phys. Rev. B* 61(3): 2371–2374.

Leem, C. S., Kim, B. J., Kim, C., Park, S. R., Ohta, T., Bostwick, A., Rotenberg, E., Kim, H. D., Kim, M. K., Choi, H. J. & Kim, C. (2008). Effect of linear density of states on the quasiparticle dynamics and small electron-phonon coupling in graphite, *Phys. Rev. Lett.* 100(1): 016802.

Mahan, G. (1990). *Many Particle Physics*, Plenum Press, New York.

Maultzsch, J., Reich, S., Thomsen, C., Requardt, H. & Ordejón, P. (2004). Phonon dispersion in graphite, *Phys. Rev. Lett.* 92(7): 075501.

Mazin, I., Boeri, L., Dolgov, O., Golubov, A., Bachelet, G., Giantomassi, M. & Andersen, O. (2007). Unresolved problems in superconductivity of CaC_6, *Physica C: Superconductivity* 460-462: 116–120.
URL: *http://dx.doi.org/10.1016/j.physc.2007.03.276*

Mazin, I. I. (2005). Intercalant-driven superconductivity in YbC_6 and CaC_6, *Phys. Rev. Lett.* 95(22): 227001.

McChesney, J. L., Bostwick, A., Ohta, T., Emtsev, K. V., Seyller, T., Horn, K. & Rotenberg, E. (2007). Massive enhancement of electron-phonon coupling in doped graphene by an electronic singularity, p. 8.
URL: *http://arxiv.org/abs/0705.3264*

McChesney, J. L., Bostwick, A., Ohta, T., Seyller, T., Horn, K., González, J. & Rotenberg, E. (2010). Extended van hove singularity and superconducting instability in doped graphene, *Phys. Rev. Lett.* 104(13): 136803.

McMillan, W. L. (1968). Transition temperature of strong-coupled superconductors, *Phys. Rev.* 167(2): 331–344.

Pan, Z.-H., Camacho, J., Upton, M. H., Fedorov, A. V., Walters, A. C., Howard, C. A, Ellerby, M. & Valla, T. (2010). Why is KC8 a superconductor and LiC6 is not? URL: http://arxiv.org/abs/1003.3903.

Park, C.-H., Giustino, F., Cohen, M. L. & Louie, S. G. (2007). Velocity renormalization and carrier lifetime in graphene from the electron-phonon interaction, *Phys. Rev. Lett.* 99(8): 086804.

Park, C.-H., Giustino, F., McChesney, J. L., Bostwick, A., Ohta, T., Rotenberg, E., Cohen, M. L. & Louie, S. G. (2008). Van hove singularity and apparent anisotropy in the electron-phonon interaction in graphene, *Phys. Rev. B* 77(11): 113410.

Posternak, M., Baldereschi, A., Freeman, A. J., Wimmer, E. & Weinert, M. (1983). Prediction of electronic interlayer states in graphite and reinterpretation of alkali bands in graphite intercalation compounds, *Phys. Rev. Lett.* 50(10): 761–764.

Pruvost, S., Herold, C., Herold, A. & Lagrange, P. (2004). Co-intercalation into graphite of lithium and sodium with an alkaline earth metal, *Carbon* 42(8-9): 1825–1831.
URL: *http://linkinghub.elsevier.com/retrieve/pii/S0008622304002106*

Smith, R. P., Kusmartseva, A., Ko, Y. T. C., Saxena, S. S., Akrap, A., Forró, L., Laad, M., Weller, T. E., Ellerby, M. & Skipper, N. T. (2006). Pressure dependence of the superconducting transition temperature in C_6Yb and C_6Ca , *Phys. Rev. B* 74(2): 024505.

Sugawara, K., Sato, T. & Takahashi, T. (2008). Fermi-surface-dependent superconducting gap in C_6Ca, *Nature Physics* 5(1): 40–43.
URL: *http://www.nature.com/doifinder/10.1038/nphys1128*

Valla, T. (2006). Comment on "Multiple bosonic mode coupling in the electron self-energy of $(La_{2-x}Sr_x)CuO_4$", *Phys. Rev. Lett.* 96(11): 119701.

Valla, T., Camacho, J., Pan, Z.-H., Fedorov, A. V., Walters, A. C., Howard, C. A. & Ellerby, M. (2009). Anisotropic electron-phonon coupling and dynamical nesting on the graphene sheets in superconducting CaC_6 using angle-resolved photoemission spectroscopy, *Phys. Rev. Lett.* 102(10): 107007.

Valla, T., Fedorov, A. V., Johnson, P. D., Glans, P.-A., McGuinness, C., Smith, K. E., Andrei, E. Y. & Berger, H. (2004). Quasiparticle spectra, charge-density waves, superconductivity, and electron-phonon coupling in 2H-NbSe$_2$, *Phys. Rev. Lett.* 92(8): 086401.

Valla, T., Fedorov, A. V., Johnson, P. D. & Hulbert, S. L. (1999). Many-body effects in angle-resolved photoemission: quasiparticle energy and lifetime of a Mo(110) surface state, *Phys. Rev. Lett.* 83(10): 2085–2088.

Valla, T., Fedorov, A. V., Johnson, P. D., Xue, J., Smith, K. E. & DiSalvo, F. J. (2000). Charge-density-wave-induced modifications to the quasiparticle self-energy in 2H-TaSe$_2$, *Phys. Rev. Lett.* 85(22): 4759–4762.

Weller, T. E., Ellerby, M., Saxena, S. S., Smith, R. P. & Skipper, N. T. (2005). Superconductivity in the intercalated graphite compounds C_6Yb and C_6Ca, *Nature Physics* 1(1): 39–41.
URL: *http://dx.doi.org/10.1038/nphys0010*
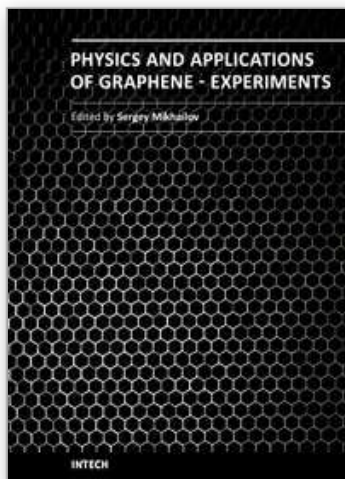
Physics and Applications of Graphene - Experiments

Edited by Dr. Sergey Mikhailov

The Stone Age, the Bronze Age, the Iron Age... Every global epoch in the history of the mankind is characterized by materials used in it. In 2004 a new era in material science was opened: the era of graphene or, more generally, of two-dimensional materials. Graphene is the strongest and the most stretchable known material, it has the record thermal conductivity and the very high mobility of charge carriers. It demonstrates many interesting fundamental physical effects and promises a lot of applications, among which are conductive ink, terahertz transistors, ultrafast photodetectors and bendable touch screens. In 2010 Andre Geim and Konstantin Novoselov were awarded the Nobel Prize in Physics "for groundbreaking experiments regarding the two-dimensional material graphene". The two volumes Physics and Applications of Graphene - Experiments and Physics and Applications of Graphene - Theory contain a collection of research articles reporting on different aspects of experimental and theoretical studies of this new material.

How to reference

In order to correctly reference this scholarly work, feel free to copy and paste the following:

INTECH
open science | open minds